Thermoelectric properties of gated phosphorene junctions

K. J. Lamas-Martínez [1], J. A. Briones-Torres [2], S. Molina-Valdovinos [1,*], and I. Rodríguez-Vargas [1,†]

[1]*Unidad Académica de Ciencia y Tecnología de la Luz y la Materia, Universidad Autónoma de Zacatecas, Circuito Marie Curie S/N, Parque de Ciencia y Tecnología QUANTUM Ciudad del Conocimiento, 98160 Zacatecas, Zacatecas, México*

[2]*Ingeniería en Nanotecnología, Universidad de La Ciénega del Estado de Michoacán de Ocampo, Avenida Universidad 3000, Col. Lomas de la Universidad, 59103 Sahuayo, Michoacán, México*

The reduced dimensions of nanostructures offer opportunities to control and improve the performance of thermoelectric devices based on two-dimensional materials. Here, we investigate theoretically the thermoelectric properties of gated phosphorene junctions (GPJs). We focus on the electronic contribution due to the possible ultralow phononic thermal conductivity in GPJs. The effects of nanostructuration, temperature, and phosphorene anisotropy are analyzed. The hybrid matrix method and the Landauer-Büttiker formalism are implemented to obtain the transmission coefficient and thermoelectric properties, respectively. We consider electronic transport mediated by holes or equivalently $n-p-n$ transport, finding that nanostructuration induces a strong anisotropy in all thermoelectric properties. The Seebeck coefficient, figure of merit, and efficiency have a better response in the zigzag direction, whereas, the electronic conductance, power factor and electronic thermal conductance have higher values in the armchair direction. In the case of large chemical potentials, large electrostatic potentials and narrow barriers the temperature generates an increase and broadening in all thermoelectric properties. In the zigzag direction, the figure of merit attains values above the technological limit value $ZT = 3$, owing to the significant reduction of the ratio of conductances with respect to the Wiedemann-Franz law and the large values of the Seebeck coefficient. On the contrary, for low chemical potentials, small electrostatic potentials and wide barriers the thermoelectric properties diminish with the temperature. In this case, the figure of merit is dictated essentially by the Seebeck coefficient due to the slight variation of the ratio of conductances with respect to the Wiedemann-Franz law.

I. INTRODUCTION

In the past years, phosphorene has become very important due to the potential applications in electronic, optoelectronic, photovoltaics, photodetectors, and spintronics [1–4]. Since 2014, phosphorene has been synthesized by means of different techniques, such as mechanical exfoliation, liquid phase exfoliation, electrochemical exfoliation, pulse laser deposition, etc. [2,5,6]. Phosphorene has a puckered-anisotropic crystalline structure with armchair (AC) and zigzag (ZZ) as main directions. Phosphorene physical properties are drastically different in these two directions [7,8]. Phosphorene has asymmetric conduction and valence bands along the AC and ZZ directions, consequently, the effective masses for electrons and holes are different in these directions [9]. Additionally, it exhibits a direct wide band gap at the Γ point of the Brillouin zone that can be tuned [7] with the number of layers [10,11], a perpendicular electric field [12], strain [13], or by controlled oxidation [14]. Phosphorene also possesses a considerable anisotropic carrier mobility. The electron mobility is substantially higher (14 times) in the AC direction, whereas, the hole mobility is greater in the ZZ direction [9]. The thermal

conductivity of phosphorene is low compared to graphene with higher values in the ZZ direction than in the AC direction [15–21]. Furthermore, the thermal conductivity is lower in monolayer black phosphorus (phosphorene) than in bulk phosphorus [22]. Recent advances on the thermal transport in 2D materials, including phosphorene, can be consulted elsewhere [23,24].

In this context, phosphorene is considered one of the most promising two-dimensional (2D) materials in the area of thermoelectricity and related potential applications, such as thermoelectric generators and thermoelectric coolers [25–27]. Thermoelectricity is a concept that is referred to converting heat energy into an electric current and vice versa. The improvement of the figure of merit (ZT) is fundamental to optimize the efficiency of the energy conversion. In phosphorene, there are several studies devoted to the determination and improvement of the thermoelectric response. From the experimental standpoint, an anisotropic figure of merit with extremely low values due to the high thermal conductivity and low electronic conductivity of the samples used is reported [28,29]. ZT values of about 0.0036 and 0.0006 were obtained for the AC and ZZ directions, respectively [25]. By controlling the carrier density through ion-gated techniques, the electronic response was enhanced [30]. In particular, the Seebeck coefficient (S) reached values up to $510\,\mu\text{V K}^{-1}$. Despite this enhancement, the ZT values still remain low.

*sergiomv@uaz.edu.mx
†isaac@uaz.edu.mx

From the theoretical side, there are multiple reports exploring strategies to improve the thermoelectric properties. For instance, upon doping it was found that phosphorene could be a good thermoelectric [31–34]. First-principles calculations predict a $ZT = 1.5$ at room temperature for both n- and p-type-doped phosphorene owing to the orthogonality between the electrical and the thermal conductances [31]. Similar calculations find an anisotropic electrical conductivity and an almost isotropic Seebeck coefficient [32]. In addition, at room temperature and optimal doping level, phosphorene presents a large thermoelectric power factor of 138.9 μW cm^{-1} K^{-2} and a $ZT = 0.3$, the latter obtained using the lattice thermal conductivity of bulk black phosphorous. The thermelectric properties of phosphorene were also studied in the presence of charge impurities [33]. A highly anisotropic electric conductivity and nearly isotropic Seebeck coefficient and figure of merit were found. At low temperatures ($T \approx 20$ K), the figure of merit reached values of $ZT = 1.2$. Another possibility that has resulted effective in improving the thermoelectric properties of phosphorene is strain engineering [35,36]. In particular, the thermoelectric properties of phosphorene are greatly enhanced by strain-induced band convergence [35]. When uniaxial strain is applied along the ZZ direction, both the electrical conductivity and the Seebeck coefficient in the ZZ direction are enhanced at a critical strain of 5%, precisely the value at which the band convergence occurs. In this case, the maximum figure of merit achieved at room temperature is $ZT = 1.67$, obtained from the bulk thermal conductivity. When the uniaxial strain is applied along the AC direction, the room-temperature figure of merit in the AC direction reaches values of $ZT = 2.12$ at a critical strain of 8%. Similar computations predict a significant enhancement of the power factor in phosphorene under tensile strain [36]. Nanostructuration also constitutes a possibility to improve the thermoelectric response of phosphorene. One of the most attractive options is nanoribbons under different configurations [37–40]. In fact, AC-phosphorene nanoribbons can reach ZT values up to 6.4 [37].

Here, it is important to mention that most of the mentioned studies were performed in the diffusive regime using the Boltzmann transport theory. However, there are also reports analyzing the thermoelectric properties of phosphorene in the ballistic transport regime using nonequilibrium Green's function transport techniques [38–43]. Highly anisotropic thermoelectric properties, except the Seebeck coefficient, were obtained [41]. The electronic conductance, electronic thermal conductance, and figure of merit are greater in the AC direction, whereas, the phonon thermal conductance is greater in the ZZ direction. The thermoelectric properties are also sensitively dependent on the chemical potential, except for the phonon thermal conductance, which is constant. The electronic conductances are greatly reduced inside the band gap and increase rapidly beyond the edges of the band gap. In contrast, the Seebeck coefficient is preponderant inside the band gap and negligible beyond the edges of the band gap. Furthermore, the electronic thermal conductance surpasses the phonon thermal conductance when the chemical potential is large. However, inside the band gap, the thermal transport is dictated by the phonon contribution. The figure of merit presents maximums at the edges of the band gap as

a result of the reduction of the Seebeck coefficient and the increase in the electronic conductances. The figure of merit is significantly higher in the AC direction, mainly due to the higher phononic thermal conductance in the ZZ direction with maximum ZT values of 0.2 at room temperature. Here, it is important to remark that the maxima of the figure of merit are related to the reduction of the ratio of electronic conductances with respect to the Lorentz number (Wiedemann-Franz law). Thus, the violation of the Wiedemann-Franz law can be used as a sign of thermoelectric response enhancement. Similar studies indicate that phosphorene at the nanoscale (ballistic transport regime) could be an option as a thermoelectric material [42,43]. In this context, phosphorene on the nanoscale in combination with an external modulating effect are quite attractive to improve the thermoelectric properties. That is the case of gated phosphorene junctions (GPJs) [44,45], which are nanostructures that can combine an external electric field (electrostatic gating) and ballistic transport. These structures are quite attractive from both the fundamental [46–50] and technological standpoints [50–53]. However, there are no reports studying the thermoelectric properties of GPJs.

In this paper, we study the thermoelectric properties of GPJs. We implement the hybrid matrix method to obtain the transmittance. With the transmittance and the Landauer-Bütiker formalism, we compute the conductance and the thermoelectric properties of GPJs. The main effects of the nanostructuration, temperature and phosphorene anisotropy on the electronic conductance, Seebeck coefficient, power factor, electronic thermal conductance, figure of merit, and efficiency of GPJs are analyzed.

The paper is organized as follows. In Sec. II, the hybrid matrix method and the thermoelectric transport coefficients are introduced. In Sec. III, the main results of the thermoelectric properties of GPJs are presented and discussed. Finally, Sec. IV contains the conclusions.

II. METHODOLOGY

Phosphorene is a 2D material conformed of phosphorus atoms arranged in a puckered structure as shown in Fig. 1(a). This special structure is the result of the sp^3 hybridization of the phosphorus atoms. The projection over the xy plane shows a honeycomb lattice with lattice vectors $a = 4.42$ and $b = 3.27$ Å in the armchair and zigzag directions, respectively, see Fig. 1(b). The distance between the two atoms in the unit cell is $\delta = 0.8$ Å and the hopping energies between the nearest-neighbor atoms are $t_1 = -1.22$ and $t_2 = 3.665$ eV.

The electron transport through a phosphorene electrostatic barrier is considered along the ZZ direction without loss of generality. A similar procedure can be applied to the AC direction. In the present case, the charge carriers propagate along the y direction, and an electrostatic gate is placed over the phosphorene layer oriented in the transverse direction, Fig. 1(c). The top gate induces an electrostatic potential of width d_B and strength V_0. This potential shifts the conduction and valence bands, Fig. 1(d). Additionally, two contacts are placed at the left/right ends, the left contact is subjected to a heat source, the right is subjected to a cold source, and a temperature gradient is generated. To describe the electronic transport across GPJs, we employ the low-energy
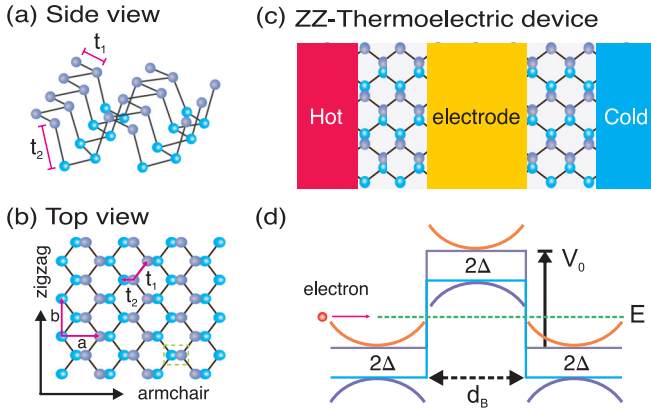
(a) Side view

(c) ZZ-Thermoelectric device

(b) Top view

(d)

FIG. 1. Illustration of the phosphorene structure: (a) side and (b) top views with t_1 and t_2 representing the nearest-neighbor interaction energies, and a and b as the lattice vectors in the AC and ZZ directions, respectively. (c) Schematic of the thermoelectric device along the ZZ direction. An electrode is placed over the phosphorene layer, and with it an electric field is applied. Two contacts with hot/cold source are placed at the left/right ends. (d) Band-edge profile of GPJs. The potential V_0 shifts the conduction and valence bands, 2Δ is the band gap, E is the energy of an incident electron, and d_B is the width of the barrier.

tight-binding Hamiltonian near the Γ point [54–56], namely,

$$
H = \begin{bmatrix} V_0 & \Delta + \frac{p_x^2}{2m_x} + \frac{p_y^2}{2m_y} - iv p_x \\ \Delta + \frac{p_x^2}{2m_x} + \frac{p_y^2}{2m_y} + iv p_x & V_0 \end{bmatrix},
$$
(1)

where $2\Delta = 4t_1 + 2t_2 = 2.45$ eV is the direct band gap, $m_x = 2\hbar^2/[-t_1 a^2 + 2\delta(2at_1 - \delta\Delta)]$ and $m_y = 2\hbar^2/(-t_1 b^2)$ are the effective masses along the AC and ZZ directions, $\vec{p} = (p_x, p_y)$ is the two-dimensional wave vector, and $v = (at_1 - \delta\Delta)/\hbar$.

The energy spectrum in the potential region is

$$
E = V_0 \pm \sqrt{\left(\Delta + \frac{\hbar^2 q_x^2}{2m_x} + \frac{\hbar^2 q_y^2}{2m_y}\right)^2 + \hbar^2 v^2 q_x^2}.
$$
(2)

To study the thermoelectric properties of GPJs, it is necessary to know the electric current and the electronic heath fluxes. With these quantities, we can find the so-called transport coefficients. These coefficients depend on the transmittance ($\mathbb{T}$) of the electrons across the device. The transmittance is obtained with the help of the hybrid matrix method [57,58]. We start the method proposing a wave function of the form

$$
\psi(x, y) = \mathbf{F}(y) e^{i q_x x},
$$
(3)

with $\mathbf{F}(y)$ as the wave function in the y direction. The next step is to substitute the wave function in the eigenvalues equation $H\psi = E\psi$. After some algebraic manipulation, it is possible to write this equation in the form of the Sturm-Liouville matrix equation [59],

$$
\mathbf{L}(y) \cdot \mathbf{F}(y) = \frac{d\mathbf{A}(y)}{dy} + \mathbf{Y}(y) \cdot \frac{d\mathbf{F}(y)}{dy} + \mathbf{W}(y) \cdot \mathbf{F}(y) = \mathbf{0},
$$
(4)

where $\mathbf{A}(y) = \mathbf{B}(y) \cdot \frac{d\mathbf{F}(y)}{dy} + \mathbf{P}(y) \cdot \mathbf{F}(y)$ is the linear differential operator, the matrices $\mathbf{B}(y)$, $\mathbf{P}(y)$, $\mathbf{Y}(y)$, and $\mathbf{W}(y)$ are given by

$$
\mathbf{B}(y) = -\frac{\hbar^2}{2m_y} \begin{bmatrix} 0 & 1 \\ 1 & 0 \end{bmatrix},
$$
(5)

$$
\mathbf{P}(y) = \mathbf{Y}(y) = 0,
$$
(6)

$$
\mathbf{W}(y) = \begin{bmatrix} V_0 - E & \Delta + \frac{\hbar^2 q_x^2}{2m_x} - iv\hbar q_x \\ \Delta + \frac{\hbar^2 q_x^2}{2m_x} + iv\hbar q_x & V_0 - E \end{bmatrix}.
$$
(7)

Then, we propose a general solution given by $\mathbf{F}(y) = \sum_{j=1}^{4} a_j \mathbf{F}_j(y)$ and $\mathbf{A}(y) = \sum_{j=1}^{4} a_j \mathbf{A}_j(y)$ where the wave function and the associated linear form are

$$
\mathbf{F}_j(y) = \mathbf{F}_{j0} e^{i q_j y} = \begin{vmatrix} \phi_{j0} \\ \varphi_{j0} \end{vmatrix} e^{i q_j y},
$$
(8)

$$
\mathbf{A}_j(y) = \mathbf{A}_{j0} e^{i q_j y} = \begin{vmatrix} \alpha_{j0} \\ \beta_{j0} \end{vmatrix} e^{i q_j y},
$$
(9)

here q_j ($j = 1$–4) are the eigenvalues, given by: $q_1 = \sqrt{-\lambda_1 + \lambda_2}$, $q_2 = -q_1$, $q_3 = i\sqrt{\lambda_1 + \lambda_2}$, and $q_4 = -q_3$, with $\lambda_1 = (2m_y/\hbar^2)(\Delta + \hbar^2 q_x^2/2m_x)$, and $\lambda_2 = (2m_y/\hbar^2)\sqrt{(E - V_0)^2 - v^2\hbar^2 q_x^2}$. The amplitudes $\mathbf{F}_{j0}$ and $\mathbf{A}_{j0}$ are

$$
\mathbf{F}_{j0} = \begin{vmatrix} \Delta + \frac{\hbar^2 q_x^2}{2m_x} + \frac{\hbar^2 q_j^2}{2m_y} - iv\hbar q_x \\ E - V_0 \end{vmatrix},
$$
(10)

$$
\mathbf{A}_{j0} = \begin{vmatrix} -\frac{i\hbar^2 q_j}{2m_y}(E - V_0) \\ -\frac{i\hbar^2 q_j}{2m_y}\left(\Delta + \frac{\hbar^2 q_x^2}{2m_x} + \frac{\hbar^2 q_j^2}{2m_y} - iv\hbar q_x\right) \end{vmatrix}.
$$
(11)

Now, we can apply the hybrid matrix method [58]. This method relates the field and linear differential form on the left side of the potential barrier [$\mathbf{F}_L(y_l)$ and $\mathbf{A}_L(y_l)$] with their corresponding ones on the right side [$\mathbf{F}_R(y_r)$ and $\mathbf{A}_R(y_r)$] in mix fashion by means of the hybrid matrix $\mathbf{H}(y_r, y_l)$, namely,

$$
\begin{vmatrix} \mathbf{F}_L(y_l) \\ \mathbf{A}_R(y_r) \end{vmatrix} = \mathbf{H}(y_r, y_l) \begin{vmatrix} \mathbf{A}_L(y_l) \\ \mathbf{F}_R(y_r) \end{vmatrix},
$$
(12)

where y_l and y_r are the limits of the barrier. The hybrid matrix $\mathbf{H}(y_r, y_l)$ for an electrostatic barrier of width $d = d_B$ is

$$
\mathbf{H}(d) = \begin{bmatrix} \phi_{10} & \phi_{20} & \phi_{30} e^{i q_3 (-d)} & \phi_{40} e^{i q_4 (-d)} \\ \varphi_{10} & \varphi_{20} & \varphi_{30} e^{i q_3 (-d)} & \varphi_{40} e^{i q_4 (-d)} \\ \alpha_{10} e^{i q_1 (d)} & \alpha_{20} e^{i q_2 (d)} & \alpha_{30} & \alpha_{40} \\ \beta_{10} e^{i q_1 (d)} & \beta_{20} e^{i q_2 (d)} & \beta_{30} & \beta_{40} \end{bmatrix} \begin{bmatrix} \alpha_{10} & \alpha_{20} & \alpha_{30} e^{i q_3 (-d)} & \alpha_{40} e^{i q_4 (-d)} \\ \beta_{10} & \beta_{20} & \beta_{30} e^{i q_3 (-d)} & \beta_{40} e^{i q_4 (-d)} \\ \phi_{10} e^{i q_1 (d)} & \phi_{20} e^{i q_2 (d)} & \phi_{30} & \phi_{40} \\ \varphi_{10} e^{i q_1 (d)} & \varphi_{20} e^{i q_2 (d)} & \varphi_{30} & \varphi_{40} \end{bmatrix}^{-1},
$$
(13)

For the regions without potential, we only take $V_0 = 0$, $q_j \to k_j$, and $q_x \to k_x$. The field ($\mathbf{F}_{L,R}$) and linear differential form ($\mathbf{A}_{L,R}$) for left and right semi-infinite regions can be written as

$$\mathbf{F}_{L,R}(y) = \sum_{j=1}^{4} a_j \begin{vmatrix} \phi_{j0W} \\ \varphi_{j0W} \end{vmatrix} e^{ik_j(y - y_{l,r})}, \tag{14}$$

$$\mathbf{A}_{L,R}(y) = \sum_{j=1}^{4} a_j \begin{vmatrix} \alpha_{j0W} \\ \beta_{j0W} \end{vmatrix} e^{ik_j(y - y_{l,r})}, \tag{15}$$

where $a_j = L_j, R_j$ are the coefficients for the left and right semi-infinite regions. The subscript W indicates the amplitudes of the region without potential. To have a physical acceptable wave function on the left/right side of the barrier, we set $L_3 = 0$ and $R_4 = 0$. On the right side, there are no waves reflected, then $R_2 = 0$. Evaluating on the left side $y = y_l$, and on the right side $y = y_r$, we obtain

$$\mathbf{F}_L(y_l) = L_1 \begin{vmatrix} \phi_{10W} \\ \varphi_{10W} \end{vmatrix} + L_2 \begin{vmatrix} \phi_{20W} \\ \varphi_{20W} \end{vmatrix} + L_4 \begin{vmatrix} \phi_{40W} \\ \varphi_{40W} \end{vmatrix}, \tag{16}$$

$$\mathbf{A}_L(y_l) = L_1 \begin{vmatrix} \alpha_{10W} \\ \beta_{10W} \end{vmatrix} + L_2 \begin{vmatrix} \alpha_{20W} \\ \beta_{20W} \end{vmatrix} + L_4 \begin{vmatrix} \alpha_{40W} \\ \beta_{40W} \end{vmatrix}, \tag{17}$$

$$\mathbf{F}_R(y_r) = R_1 \begin{vmatrix} \phi_{10W} \\ \varphi_{10W} \end{vmatrix} + R_3 \begin{vmatrix} \phi_{30W} \\ \varphi_{30W} \end{vmatrix}, \tag{18}$$

$$\mathbf{A}_R(y_r) = R_1 \begin{vmatrix} \alpha_{10W} \\ \beta_{10W} \end{vmatrix} + R_3 \begin{vmatrix} \alpha_{30W} \\ \beta_{30W} \end{vmatrix}. \tag{19}$$

By substituting $\mathbf{H}(y_r, y_l)$, $\mathbf{F}_{L,R}(y_{l,r})$, and $\mathbf{A}_{L,R}(y_{l,r})$ in Eq. (12), we get

$$\begin{vmatrix} L_2/L_1 \\ L_4/L_1 \\ R_1/L_1 \\ R_3/L_1 \end{vmatrix} = [M_1 - \mathbf{H}(y_r, y_l) \cdot M_2]^{-1} [\mathbf{H}(y_r, y_l) \cdot M_3 - M_4], \tag{20}$$

where the auxiliary matrices M_1, M_2, M_3, and M_4 are given by

$$M_1 = \begin{bmatrix} \phi_{20W} & \phi_{40W} & 0 & 0 \\ \varphi_{20W} & \varphi_{40W} & 0 & 0 \\ 0 & 0 & \alpha_{10W} & \alpha_{30W} \\ 0 & 0 & \beta_{10W} & \beta_{30W} \end{bmatrix}, \tag{21}$$

$$M_2 = \begin{bmatrix} \alpha_{20W} & \alpha_{40W} & 0 & 0 \\ \beta_{20W} & \beta_{40W} & 0 & 0 \\ 0 & 0 & \phi_{10W} & \phi_{30W} \\ 0 & 0 & \varphi_{10W} & \varphi_{30W} \end{bmatrix}, \tag{22}$$

$$M_3 = \begin{vmatrix} \alpha_{10W} \\ \beta_{10W} \\ 0 \\ 0 \end{vmatrix}, \qquad M_4 = \begin{vmatrix} \phi_{10W} \\ \varphi_{10W} \\ 0 \\ 0 \end{vmatrix}. \tag{23}$$

From Eq. (20), we can obtain the relation between R_1 and L_1, which defines the transmission coefficient,

$$\mathbb{T} = \left| \frac{R_1}{L_1} \right|^2. \tag{24}$$

In the ballistic regime, the transport coefficients are derived taking into account the linear response of the applied bias and temperature. The current and heat fluxes through a thermoelectric device are found from the Landauer formalism [60],

$$I = \frac{2e}{h} \int_{-\infty}^{\infty} \mathbb{T}(E)(f_1 - f_2) dE, \tag{25}$$

$$I_Q = \frac{2e}{h} \int_{-\infty}^{\infty} \mathbb{T}(E)(f_1 - f_2) \left(\frac{E - \mu}{e} \right) dE, \tag{26}$$

here $f_1 = f_1(E, \mu_1, T_1)$ and $f_2 = f_2(E, \mu_2, T_2)$ are the Fermi functions of the right/left lead, T_1, μ_1 and T_2, μ_2 are the temperature and chemical potential of the right/left lead, and e is the electron charge.

If we consider all the impinging angles of the charge carriers, $\sum_{k_x} \mathbb{T}(E, k_x) \to (L_x/2\pi) \int \mathbb{T}(E, k_x) dk_x$. Then, the conductance at zero temperature can be written as

$$G^*(E) = G_0 \int_{k_x^{\min}}^{k_x^{\max}} \mathbb{T}(E_F, k_x) dk_x, \tag{27}$$

where $G_0 = 2e^2 L_x / 2\pi h$ with L_x as the length of the material along the x axis, E_F is the Fermi energy, h is the Planck constant, and k_x is the wave vector in the x direction. The integral is computed over the interval of relevant wave-vectors $k_x^{\min} < k_x < k_x^{\max}$.

From a Taylor series expansion of the Fermi functions $(f_1 - f_2)$ around the equilibrium point, take into account all the impinging angles of the charge carriers and under the assumption of open circuit ($I = 0$) in the linear-response regime, it is possible to deduce the Seebeck coefficient and electron thermal conductance as

$$S = \left(\frac{\Delta V}{\Delta T} \right)_{I=0} = -\frac{G_S}{G}, \tag{28}$$

$$G_K = \left(\frac{\partial I_Q}{\partial \Delta T} \right)_{I=0} = G_Q - \frac{G_P G_S}{G}, \tag{29}$$

where $G(\mu, T)$ denotes the temperature-dependent conductance given as

$$G(\mu, T) = \int_{-\infty}^{\infty} G^*(E) \left(-\frac{\partial f}{\partial E} \right) dE. \tag{30}$$

The rest of the coefficients $G_P = G_S T$, G_S, and G_Q are defined as

$$G_S(\mu, T) = \frac{1}{e} \int_{-\infty}^{\infty} G^*(E) \left(-\frac{\partial f}{\partial E} \right) \left(\frac{E - \mu}{T} \right) dE, \tag{31}$$

$$G_Q(\mu, T) = \int_{-\infty}^{\infty} G^*(E) \frac{(E - \mu)^2}{e^2 T} \left(-\frac{\partial f}{\partial E} \right) dE. \tag{32}$$

The quantity $S^2 G$ is known as the power factor, and $\Pi = ST$ is the Peltier coefficient. The figure of merit is given by

$$ZT = \frac{S^2 G T}{G_K}. \tag{33}$$

The maximum power is defined as $P_{\max} = S^2 G (\Delta T)^2/4$, and the efficiency evaluated at the maximum power is

$$\eta(P_{\max}) = \frac{\eta_c}{2} \frac{ZT}{2 + ZT}, \tag{34}$$

with $\eta_c = (T_2 - T_1)/T_2$ as the Carnot efficiency.

III. RESULTS AND DISCUSSION

In this section, we present the thermoelectric properties of GPJs. The device configuration is the one proposed in Fig. 1(c). This configuration allows electronic transport mediated by holes or $n-p-n$ transport. In the first place, we will consider high chemical potentials, large electrostatic potentials, and narrow barriers as fundamental parameters of GPJs. These parameters are typical in the literature, however, they do not correspond necessarily to realistic values for the gate-bias configuration of the device model. So, in second place, we will consider realistic parameters of GPJs. In particular, low chemical potentials, small electrostatic potentials, and wide barriers. In both cases, the temperatures will fall in the range of 0–300 K. In the case of GPJs with $n-n-n$ transport, that is, low chemical potentials, small electrostatic potentials, and wide barriers the thermoelectric properties are not so different from the pristine case except for the slight variations of the Seebeck coefficient and the ratio of conductances near the positive edge of the intrinsic phosphoren's band gap that result in an enhancement of the electronic figure of merit. The figure of merit including the phononic contribution is slightly reduced from the one corresponding to the pristine case. More details can be found in Sec. S1 of the Supplemental Material [61].

In Figs. 2–8, the main results of the thermoelectric properties of GPJs with $V_0 = 4$ eV and $d_B = 3$ nm as fundamental parameters are presented. In this case, the temperatures considered are as follows: $T = 10$ K (black line), 50 K (green line), 100 K (red line), and 200 K (blue line). Figure 2 shows the electronic conductance as a function of chemical potential for GPJs along the AC and ZZ directions. In general, the nanostructuration of the phosphorene layer induces a high anisotropic behavior in the electronic conductance. The conductance has larger values in the AC direction than in the ZZ direction. Note that the conductance has low values near the chemical potential equal to zero, indicating that the doping level or carrier concentration of the system is low. Additionally, two main gaps are observed in both directions, the first gap is located in the range of $-1.22 < \mu < 1.22$ eV, associated with the intrinsic phosphorene gap. The second gap is caused by the potential barrier and is located approximately in the range of $2.75 < \mu < 5.25$ eV. The temperature does not affect considerably the conductance in both directions, see Fig. 2(a) and 2(b). This happens due to the large value of the band gap and potential barrier. In the AC direction, the conductance presents a series of sharp peaks in the energy range of $1 < \mu < 3$ eV associated with the hole states inside the barrier, corresponding to Fabry-Pérot resonances in the transmission profiles [46]. When the temperature increases, the sharp peaks smooth out, see Fig. 2(c). In the ZZ direction, the conductance shows several singular peaks ($1 < \mu < 3$ eV) related to the energy location of invisible confined states
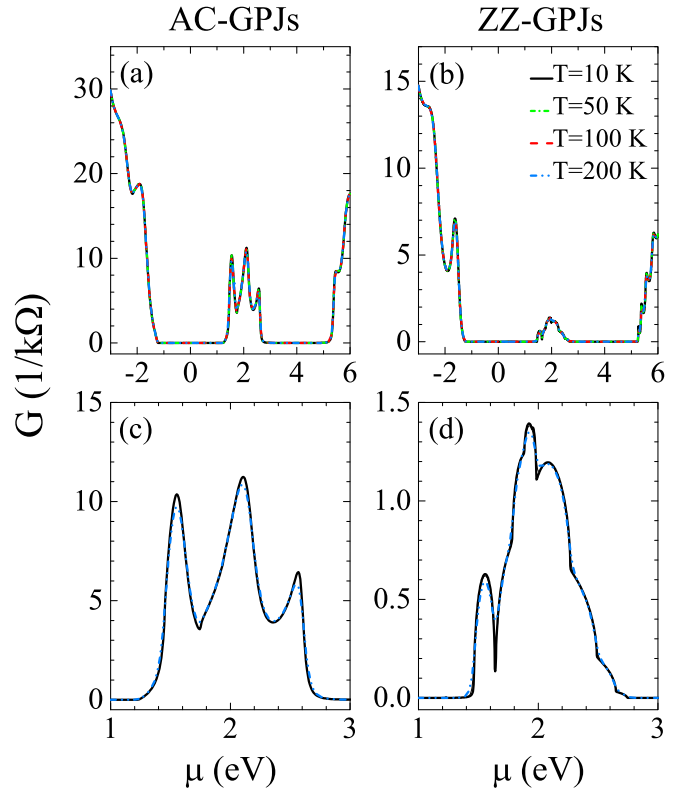

FIG. 2. Conductance as a function of the chemical potential for the (a) armchair and (b) zigzag directions. (c) and (d) correspond to zooms in the energy range of $1 < \mu < 3$ eV of (a) and (b), respectively. The parameters of the GPJs in both directions are $V_0 = 4$ eV and $d_B = 3$ nm.

(electronic cloaking) [46]. If we take a zoom of the conductance in the energy range of $1 < \mu < 3$ eV, we can see that the hallmarks of the electronic cloaking are lost as the temperature rises, see Fig. 2(d).

The Seebeck coefficient in the AC and ZZ directions as a function of the chemical potential is presented in Fig. 3. Interestingly, the Seebeck coefficient exhibits an anisotropic behavior as a result of the nanostructuration, increasing as the temperature rises. In general, the S values in the ZZ direction are ten times greater that the values in the AC direction. For both directions, the main response takes place at the edges of the second band gap. The maximum values of S at $T = 200$ K are 0.13 and 1.2 mV/K for the AC and ZZ directions, respectively. On the contrary, in the region of the intrinsic band-gap ($-1.2 < \mu < 1.2$ eV), the Seebeck coefficient shows an isotropic behavior, i.e., the S coefficient for AC and ZZ directions adopts the same values, see Figs. 3(c)–3(d). In this case, as the temperature increases, the Seebeck coefficient decreases. In addition, the values of S in this region are higher than the S values in other energy regions. Remember that the Seebeck coefficient is defined as $S = -G_S/G$, then reaching high values is possible when the electronic conductance is very low. In fact, this is what happens in the intrinsic gap region with an extremely low conductance that leads to an isotropic Seebeck coefficient that gets smaller as the temperatures increases. In particular, S reaches a maximum value near $\mu \approx 0$ and then decreases until vanishing near the edges of the
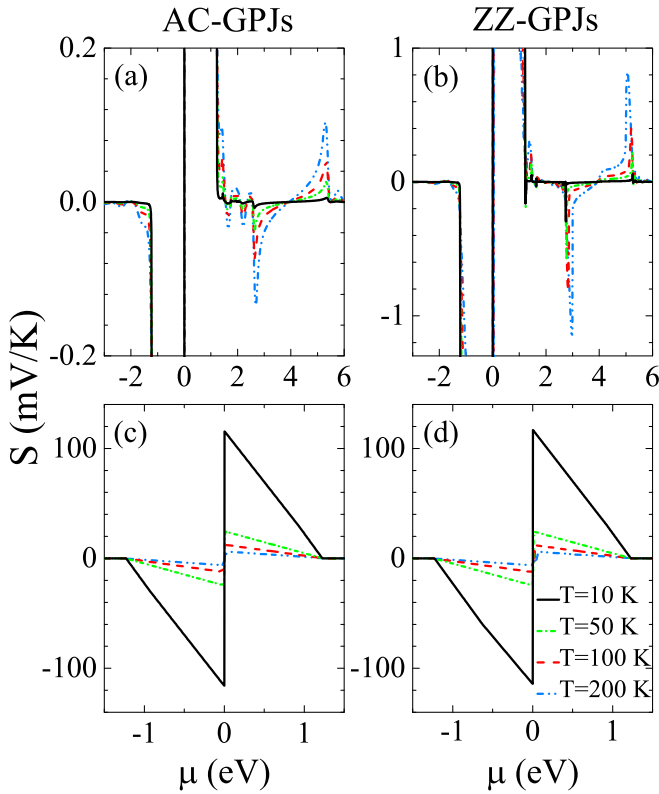
FIG. 3. Seebeck coefficient as a function of the chemical potential for the (a) armchair and (b) zigzag directions. (c) and (d) correspond to zooms in the energy range of $-1.2 < \mu < 1.2$ eV of (a) and (b), respectively. The parameters of the GPJs are the same as in Fig. 2.
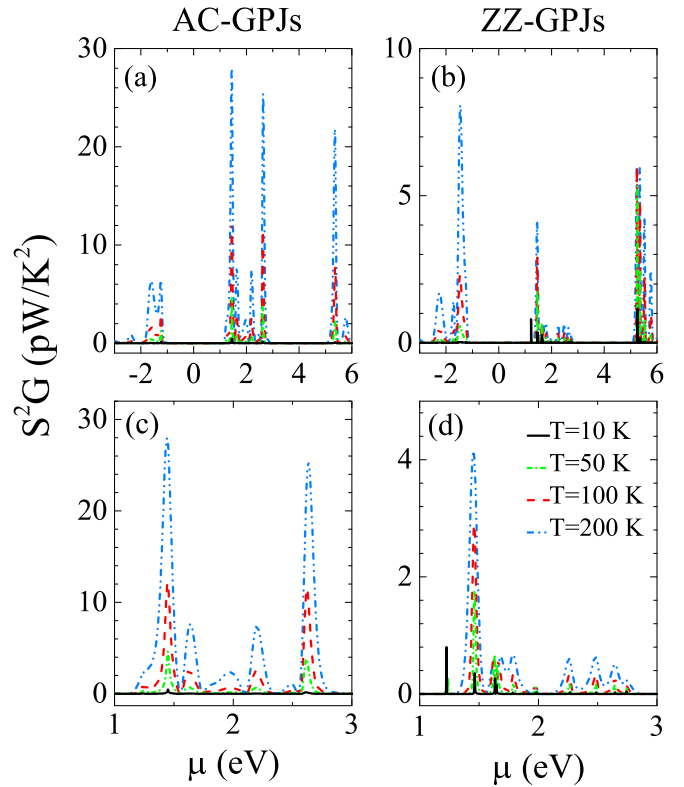

FIG. 4. Power factor as a function of chemical potential for the (a) armchair and (b) zigzag directions. (c) and (d) correspond to zooms in the energy range of $1 < \mu < 3$ eV of (a) and (b), respectively. The parameters of the GPJs are the same as in Fig. 2.

intrinsic gap. This behavior is similar to the one presented in pristine phosphorene [41]. Here, it is important to remark that despite the huge values of the Seebeck coefficient, this energy region is practically inaccessible via thermal excitation due to the energy scale of the intrinsic gap, which results in an extremely low conductance. So, hereafter we let out of our analysis the intrinsic gap region, specifically the energy region around $\mu \approx 0$. Regarding the energy range of $1 < \mu < 3$ eV, we can see that the sharp peaks in the AC direction increase and broaden as the temperature increases. In the ZZ direction, a similar dynamic is presented for the inverted peaks related to the cloaking states [46]. The details can be found in Fig. S5 of the Supplemental Material [61].

Now, with the conductance and Seebeck coefficient, we can analyze straightforwardly the power factor $S^2 G$. In Fig. 4, the main results of the power factor as a function of chemical potential for the (a) AC and (b) ZZ directions are shown. As we can note, the power factor is also anisotropic. Contrary to the Seebeck coefficient, here, the power factor attains higher values in the AC direction than in the ZZ direction. This happens due to the larger electronic conductance in the AC direction. As a comparative for the region of $1 < \mu < 3$ eV, the power factor values in the AC direction are seven times larger than in the ZZ direction, see Figs. 4(c) and 4(d). With the temperature, the power factor increases, and the power factor peaks broaden. We can also note that the power factor peaks take place at the edges of the intrinsic and secondary

gaps as well as in the energy region of the conductance peaks. In the AC direction, the dominant peaks correspond to the sharp peaks in the conductance, see Fig. 4(c), and correlate it with Fig. 2(c). These peaks are also attractive due to the considerable transport response in that energy region. In the ZZ direction, the dominant power factor peaks are located at the lower and higher edges of the intrinsic and secondary gaps, respectively. There are also important power
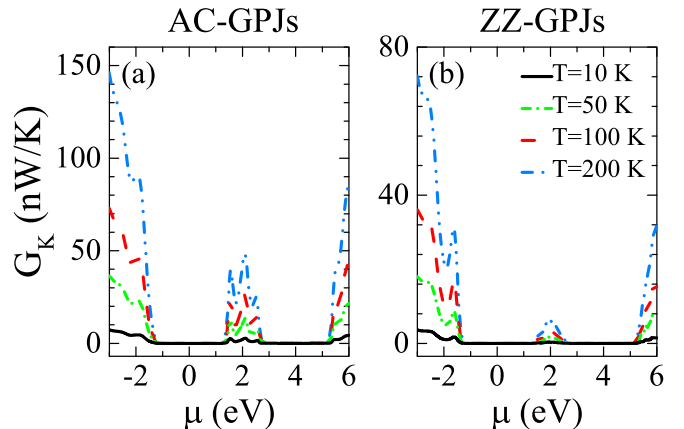

FIG. 5. Electronic thermal conductance as a function of chemical potential for the (a) armchair and (b) zigzag directions. The parameters of the GPJs are the same as in Fig. 2.

FIG. 6. Figure of merit as a function of chemical potential for the (a) armchair and (b) zigzag directions. Here, ZT is computed taking into account only the electronic contribution G_K. The parameters of the GPJs are the same as in Fig. 2.

FIG. 8. Ratio between the electronic thermal conductance and the electronic conductance as a function of chemical potential for the (a) armchair and (b) zigzag directions. The parameters of the GPJs are the same as in Fig. 2.
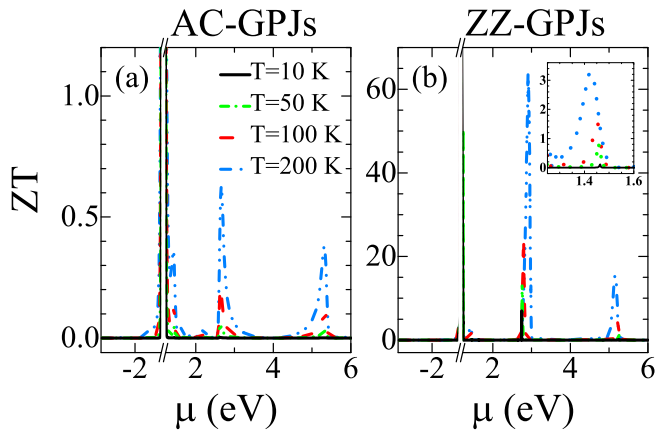
factor peaks related to the sharp peaks of the conductance, see Fig. 4(d) and correlate it with Fig. 2(d). In the intrinsic gap region, the extremely low values of the electronic conductance prevail over the values of the Seebeck coefficient, and, as a consequence, the power factor becomes negligible in this region.

The electronic thermal conductance for the AC and ZZ directions is shown in Fig. 5. As we can note, the electronic thermal conductance shows similar characteristics as the electronic conductance. First, the electronic thermal conductance is anisotropic with larger values in the AC direction than in the ZZ direction. Second, the nanostructuration gives rise to a secondary gap and a region of considerable electronic thermal conductance related to the hole states inside the barrier. As comparative, in this region $1 < \mu < 3$ eV, the electronic thermal conductance is seven times larger in the AC direction than in the ZZ direction. The increase in the temperature causes an increase in the electronic thermal conductance in both directions. It is also interesting to note that inside the intrinsic and secondary gaps, the electronic
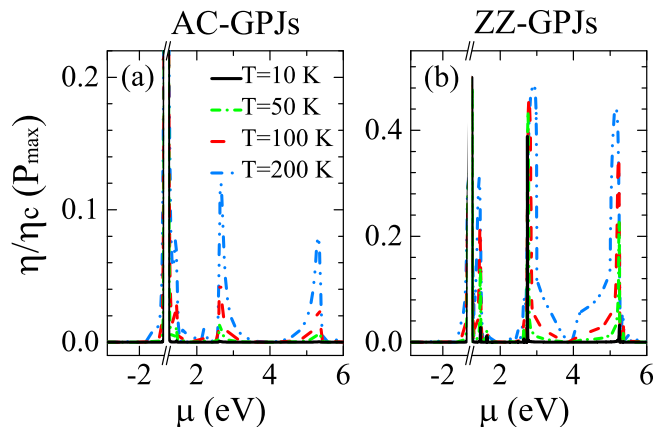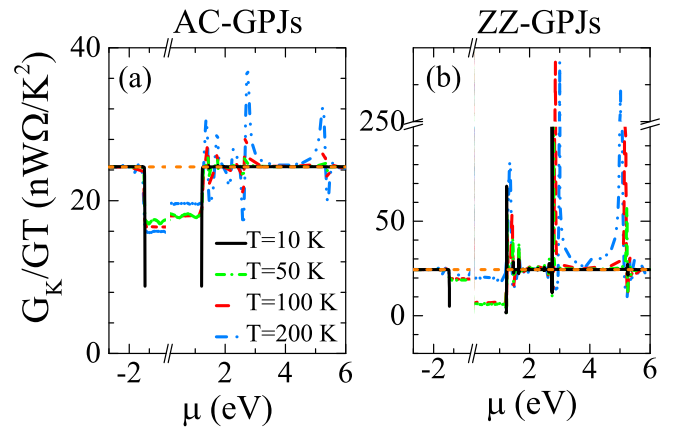

FIG. 7. Efficiency at maximum power as a function of chemical potential for the (a) armchair and (b) zigzag directions. The parameters of the GPJs are the same as in Fig. 2.

thermal conductance is negligible, reaching considerable values near the edges of both gaps. These characteristics are quite relevant because in conjunction with the power factor will determine the figure of merit and efficiency. It is also important to remark that at low temperatures, the electronic thermal conductance is the main contribution to the thermal transport. However, as the temperature rises the phonon contribution is more relevant, becoming preponderant at high temperatures as in the case of pristine phosphorene [41].

Figure 6 shows the figure of merit (ZT) as a function of chemical potential for GPJs along the (a) AC and (b) ZZ directions. In this case, the figure of merit was computed taking into account only the electronic thermal conductance (G_K). We can see that ZT exhibits an anisotropic behavior. The ZT values in the ZZ direction are significantly higher than the values in the AC direction. As the temperature increases, the ZT values increase too. The high values of ZT are located close to the edges of the intrinsic ($-1.22 < \mu < 1.22$ eV) and secondary ($2.75 < \mu < 5.25$ eV) gap. In the AC direction, the maximum ZT values at $T = 200$ K are 0.4, 0.6, and 0.4, corresponding to chemical potentials of $\mu = 1.42$, 2.7, and 5.3 eV, respectively. In the ZZ direction, the maximum ZT values are 3.3, 63, and 15.4, corresponding to $\mu = 1.42$, 2.9, and 5.2 eV, respectively. Here, it is important to remember that as the figure of merit is inversely proportional to the electronic thermal conductance extremely low values of this quantity can result in huge figures of merit. In fact, this is what happens with the peak of the figure of merit at $\mu = 2.9$ eV in the ZZ direction. However, with this particular peak we need to be cautious because it does not correspond to an optimized or considerable power factor due to the reduced electronic conductance in that energy region and, consequently, not a reliable thermoelectric response necessarily. A different story is that of the peak at $\mu = 1.42$ eV, see the inset in Fig. 6. This peak is the result of a low electronic thermal conductance and an optimized power factor. So, the thermoelectric response around this peak is, in principle, possible.

Now, with the figure of merit we can analyze readily the main characteristics of the efficiency of GPJs. In Fig. 7, the

efficiency at maximum power for the (a) AC and (b) ZZ directions is shown. As we can note, the characteristics of the efficiency are similar to those of the figure of merit. This is understandable because the efficiency depends directly on the figure of merit, see Eq. (34). Specifically, the efficiency is anisotropic with greater values in the ZZ direction than in the AC direction. In addition, the efficiency increases with the temperature, and its maximum values occur close to the edges of the intrinsic and secondary gaps. Here, it is also important to mention that for huge values of the figure of merit ($ZT \gg 2$), the efficiency (η/η_c) will tend to 0.5 as we can realize from Eq. (34). In fact, this is what happens with the peak at $\mu = 2.9$ eV in the ZZ direction, reaching an efficiency of 0.48. This efficiency is four times the value (0.12) reached by the same peak in the AC direction. The other peaks in the ZZ direction are also considerable with efficiencies above 0.3, and with possibilities due to the optimized power factor around them.

An auxiliary quantity that can help us to identify the energy region of thermoelectric optimization is the ratio between the electronic thermal conductance and the electronic conductance (G_K/GT). In metals, semiconductors, and 2D materials, this ratio adopts a constant value of 24.4 nW Ω/K^2, known as the Lorentz number and constituting the so-called Wiedemann-Franz law. So, the presence of a band gap and/or nanostructuration can cause deviations from this value. In particular, a reduction of G_K/GT with respect to the Lorentz number can result in an enhancement of the figure of merit and, consequently, of the efficiency, if the Seebeck coefficient keeps considerable or optimize values. Keep in mind that $ZT = S^2/(G_K/GT)$. The main results of G_K/GT as a function of the chemical potential for GPJs are shown in Fig. 8. As we can note, G_K/GT is anisotropic. In both directions, G_K/GT deviates from the Lorentz number (orange horizontal line) close to the edges of the intrinsic and secondary gaps as well as in the energy region of the hole states inside the barrier. This indicates that the Wiedemann-Franz law is no longer valid in that energy regions [41,62]. The deviation of G_K/GT also increases as the temperature rises. In the AC direction, the minima of G_K/GT for $T = 200$ K reach values of about 20 nW Ω/K^2 with the dominant minimum located at $\mu = 2.7$ eV. In the ZZ direction, the minima for $T = 200$ K are below 20 nW Ω/K^2 with the dominant minimum at $\mu = 5.2$ eV reaching a value of 10 nW Ω/K^2. From this analysis, we can realize that in the ZZ direction the greater reduction of G_K/GT with respect to the Lorentz number in conjunction with the greater values of the Seebeck coefficient result in large figures of merit.

Now, it is a turn to analyze the thermoelectric properties of GPJs for realistic parameters. For instance, chemical potentials up to $\mu = 0.1$ eV for both electrons and holes, electrostatic potentials of $V_0 = 0.05$ eV, and barrier widths of $d_B = 10$–200 nm. These realistic parameters allow us to analyze the impact of nanostructuration. However, due to the large phosphorene band gap is not possible to have holes participating in the electronic transport, or in other words, $n{-}p{-}n$ transport as in the case already discussed. $n{-}p{-}n$ transport can be achieved by narrowing the phosphorene band gap via an electric field [12,63–65]. According to the mentioned parameters, a band gap of 25 meV allows $n{-}p{-}n$
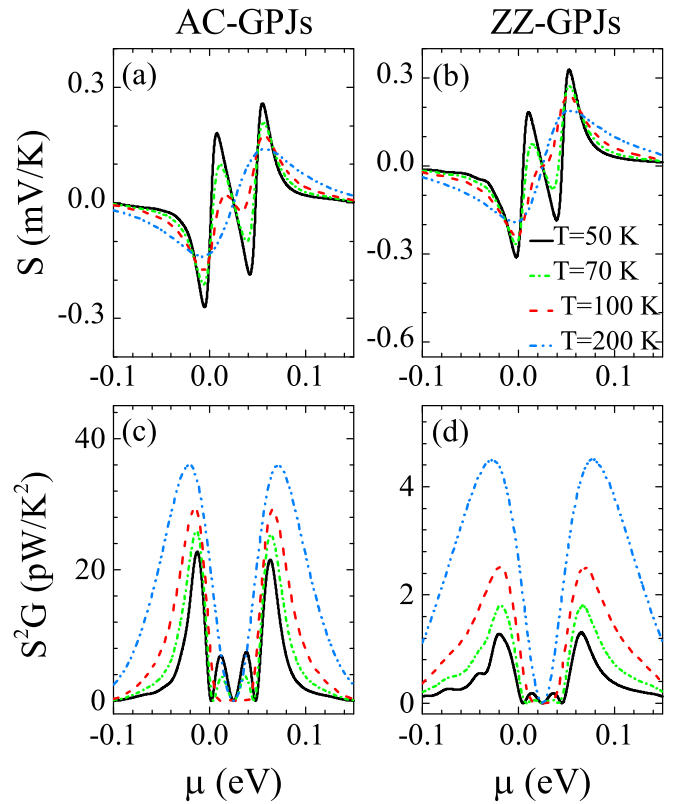

FIG. 9. Seebeck coefficient and power factor as a function of chemical potential for realistic parameters of GPJs. Chemical potentials up to $\mu = 0.1$ for electrons, holes, and electrostatic potentials of $V_0 = 0.05$ eV. The width of the barrier is $d_B = 150$ nm in the AC direction, and $d_B = 20$ nm in the ZZ direction.

transport. We find that for these realistic parameters, the thermoelectric properties present two temperatures regimes: (1) the low-temperature regime in which the thermoelectric properties increase with the temperature, and (2) the high-temperature regime for which the thermoelectric properties (except the power factor) diminish as the temperature increases. The former is similar to the case of large electrostatic barriers, large chemical potentials, and narrow barrier widths already discussed. These results are shown in Sec. S3 of the Supplemental Material [61]. The latter tells us that temperature has a huge impact on the thermoelectric properties of GPJs when realistic parameters are considered. These results are shown in Figs. 9–11. The temperatures in this case are as follows: $T = 50$ K (black line), 70 K (green line), 100 K (red line), and 200 K (blue line). The primary and secondary gaps lie between -12.5 and 12.5, 37.5, and 62.5 meV, respectively. As we can note, the peaks in the thermoelectric properties take place at the edges of the primary and secondary gaps with dominant peaks the ones at the lower and higher edge of the primary and secondary gaps, respectively. We can also see that there are no peaks related to the Fabry-Pérot resonances and the cloaking states due to the considerable redistribution of the charge carriers with the temperature. In addition, the thermoelectric properties diminish, in general, with the temperature except the power factor $S^2 G$, which increases owing to the enhancement of the electronic conductance with the
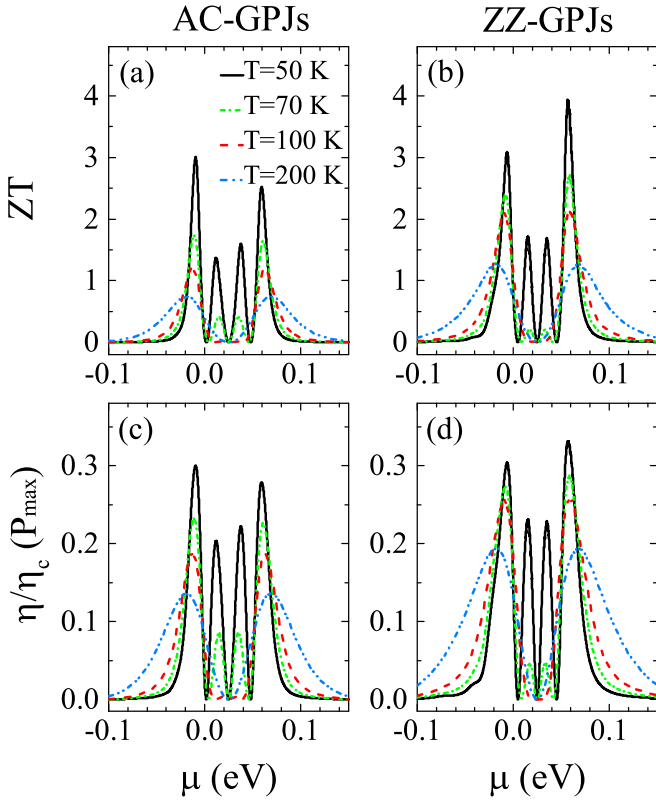
FIG. 10. Figure of merit and efficiency as a function of chemical potential for realistic parameters of GPJs. The realistic parameters are the same as in Fig. 9.

FIG. 11. Electronic conductance, electronic thermal conductance, and ration between conductances as a function of chemical potential for realistic parameters of GPJs. The realistic parameters are the same as in Fig. 9.

temperature. In the case of ZT, its characteristics are dictated essentially by S due to the slight reduction in G_K/GT with respect to the Lorentz number. In fact, ZT is larger in the ZZ direction than in the AC direction and drops in both directions as the temperature rises. ZT reaches values up to 3 and 4 in the AC and ZZ directions, respectively. These values at first instance are attractive, but they take place at $T = 50$ K. At higher temperatures ($T = 200$ K), ZT gets values around 1. Furthermore, at room-temperature ZT is reduced considerably if we include the phonon contribution, see Fig. S13 in the Supplemental Material [61]. In short, for realistic parameters of GPJs is quite relevant to reduce the temperature in order to have a good thermoelectric response. Another possibility is to have access to higher chemical potentials and higher electrostatic potentials that open the door to higher temperatures with good thermoelectric response.

Finally, we would like to remark some important issues that can affect the performance of thermoelectric devices based on GPJs. First, the phonon thermal conductance (G_{ph}) plays an important role in the thermal transport as the temperature rises, becoming the main contribution at high temperatures [41,43]. G_{ph} can be incorporated into ZT by adding it to G_K, resulting in $ZT = S^2GT/(G_K + G_{ph})$. From this relationship, we can realize that, in general, ZT will be reduced when G_{ph} is incorporated. In the case of GPJs, we expect a greater reduction of ZT in the ZZ direction due to the larger thermal conductivity of phosphorene in that direction [41]. In fact, if we use the values of the thermal conductivity reported for pristine phosphorene at high
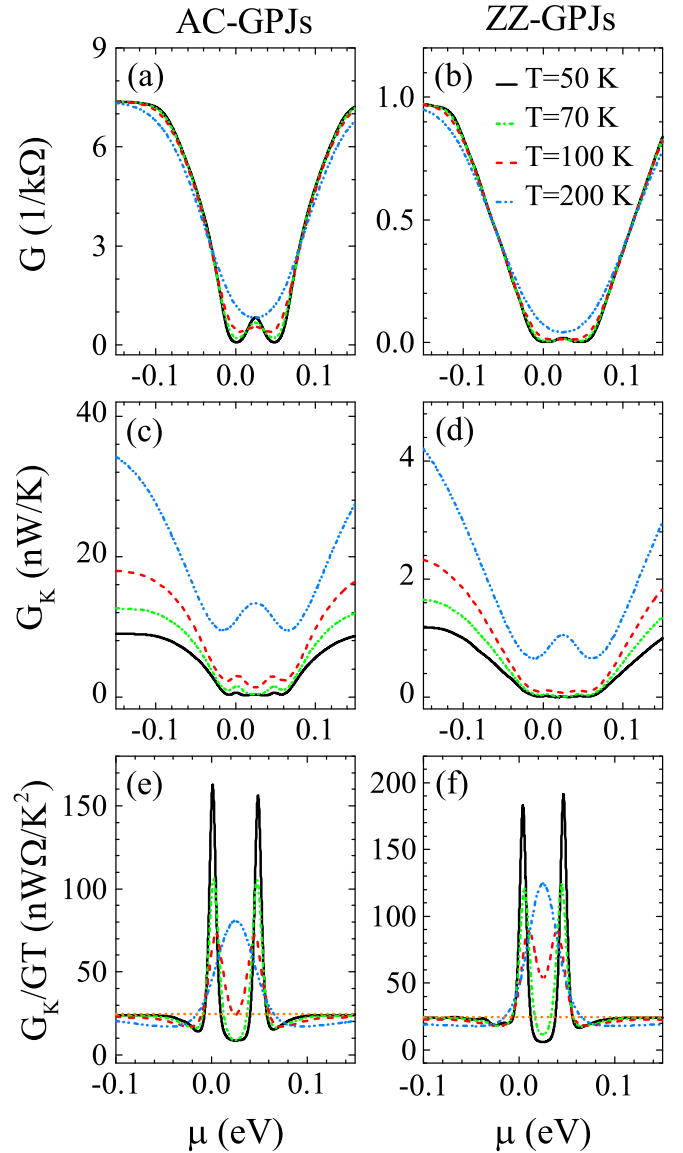
temperatures [41], a significant reduction of the figure of merit of GPJs is obtained with the greatest reduction taking place in the ZZ direction. The specific results can be seen in Fig. S14 of the Supplemental Material [61]. Second, to incorporate phosphorene into a device configuration, it is necessary a supporting substrate and protecting layers. In this regard, it is well documented that these fundamental elements of any practical device reduce considerably the thermal conductivity of 2D materials [66–70]. So, a reduction of the thermal conductivity is expected in our phosphorene thermoelectric device. Third, it is known that an applied electric field can reduce the thermal conductivity of 2D materials [71–75]. In general, the applied electric-field results in an ultralow thermal conductivity due to the renormalization of the interaction between the constituent atoms (phonon renormalization). As all these elements (supporting substrate, protecting layers and

electrostatic gating) are in play in GPJs, an ultralow thermal conductivity is plausible, and, consequently, our ZT values could be a possibility.

IV. CONCLUSIONS

To summarize, we have studied the thermoelectric properties of GPJs. The hybrid matrix method and the Landauer-Büttiker formalism were implemented to calculate the transmission coefficient and the thermoelectric properties, respectively. We focus on the energy regions affected by the nanostructuration. In particular, the edges of the intrinsic (primary) and secondary gaps as well as the energy region of hole states inside the electrostatic barrier. We have considered large chemical potentials, large electrostatic barriers, and narrow barrier widths as typical parameters in the literature for GPJs. We also consider low chemical potentials, small electrostatic barriers, and wide barrier widths as realistic parameters for GPJs. In the first case, we found that nanostructuration induces a strong anisotropy in practically all thermoelectric properties. The Seebeck coefficient, figure of merit, and efficiency have higher values in the ZZ direction, whereas, the electronic conductance, power factor, and electronic thermal conductance present higher values in the AC direction. The fundamental peaks of the thermoelectric properties take place at the edges of the intrinsic and secondary gaps as well as in the energy region of holes inside the barrier. In addition with the temperature, the thermoelectric properties increase, and the fundamental peaks broaden. In the particular case of the Seebeck coefficient, the values in the ZZ direction are ten times larger than in the AC direction. The Seebeck coefficient also presents oscillations (inverted peaks) in the energy region of hole states inside the barrier due to the Fabry-Pérot resonances (cloaking states) in the AC (ZZ) directions. The power factor reaches values three times higher in the AC direction than in the ZZ direction due to the larger electronic conductance in the AC direction. The figure of merit attains significantly higher values in the ZZ direction at the edges of the intrinsic and secondary gaps, above the technological limit value $ZT = 3$, representing an enhancement of more than an order of magnitude with respect to the ZT values in the AC direction. In the same fashion, the efficiency gets values above $\eta = 0.3\eta_c$, constituting an enhancement of more than three times with respect to the AC direction. By analyzing the ratio of conductances G_K/GT, we can realize that the regions with optimized thermoelectric response are those in which this quantity deviates from the Wiedemann-Franz law (Lorentz number). Specifically, the maximum reduction of G_K/GT is presented at the edges of the intrinsic and secondary gaps of the ZZ direction, which, in conjunction with the higher Seebeck coefficient in this direction result in a better thermoelectric response. In the second case, we found essentially the same physics as in the first case, if the temperature is appropriately adjusted (extremely low temperatures). For temperatures similar to the first case, the thermoelectric properties are greatly affected by the temperature effects. In particular, the thermoelectric properties are dictated by the primary and secondary gaps with dominant peaks at the edges of the gaps. In addition, the figure of merit and efficiency are determined essentially by the Seebeck coefficient due to the slight reduction in G_K/GT with respect to the Lorentz number. Thus, for realistic parameters of GPJs is quite relevant to reduce the temperature in order to have a good thermoelectric response. Finally, it is important to mention that the present results could be possible if the thermal conductivity is significantly reduced. In fact, this could be the case in our thermoelectric device since basic elements as the supporting substrate, protecting layers and electrostatic gating reduce, in general, the thermal conductivity.

ACKNOWLEDGMENTS

[1] J. Pang, A. Bachmatiuk, Y. Yin, B. Trzebicka, L. Zhao, L. Fu, R. G. Mendes, T. Gemming, Z. Liu, and M. H. Rummeli, Applications of phosphorene and black phosphorus in energy conversion and storage devices, Adv. Energy Mater. **8**, 1702093 (2018).

[2] M. Peruzzini, R. Bini, M. Bolognesi, M. Caporali, M. Ceppatelli, F. Cicogna, S. Coiai, S. Heun, A. Ienco, I. I. Benito, and others, A perspective on recent advances in phosphorene functionalization and its applications in devices, Eur. J. Inorg. Chem. **2019**, 1476 (2019).

[3] M. Long, P. Wang, H. Fang, and W. Hu, Progress, challenges, and opportunities for 2D material based photodetectors, Adv. Funct. Mater. **29**, 1803807 (2019).

[4] A. Carvalho, M. Wang, X. Zhu, A. S. Rodin, H. Su, A. H. Castro Neto, Phosphorene: From theory to applications, Nat. Rev. Mater. **1**, 16061 (2016).

[5] M. Akhtar, G. Anderson, R. Zhao, A. Alruqi, J. E. Mroczkowska, G. Sumanasekera, and J. B. Jasinski, Recent advances in synthesis, properties, and applications of phosphorene, npj 2D Mater. Appl. **1**, 5 (2017).

[6] S. Zhang, S. Guo, Z. Chen, Y. Wang, H. Gao, J. Gómez-Herrero, P. Ares, F. Zamora, Z. Zhu, and H. Zeng, Recent progress in 2D group-VA semiconductors: From theory to experiment, Chem. Soc. Rev. **47**, 982 (2018).

[7] A. Castellanos-Gomez, Black phosphorus: Narrow gap, wide applications, J. Phys. Chem. Lett. **6**, 4280 (2015).

[8] X. J. Li, J. H. Yu, K. Luo, Z. H. Wu and W. Yang, Tuning the electrical and optical anisotropy of a monolayer black phosphorus magnetic superlattice, Nanotechnology **29**, 174001 (2018).

[9] J. Qiao, X. Kong, Z. X. Hu, F. Yang, and W. Ji, High-mobility transport anisotropy and linear dichroism in few-layer black phosphorus, Nat. Commun. **5**, 4475 (2014).

[10] A. Castellanos-Gomez, L. Vicarelli, E. Prada, J. O. Island, K. L. Narasimha-Acharya, S. I. Blanter, D. J. Groenendijk, M. Buscema, G. A. Steele, J. V. Alvarez, H. W. Zandbergen, J. J. Palacios and H. S. J. van der Zant, Isolation and characterization of few-layer black phosphorus, 2D Mater. **1**, 025001 (2014).

[11] Y. Cai, G. Zhang, and Y. W. Zhang, Layer-dependent band alignment and work function of few-layer phosphorene, Sci. Rep. **4**, 6677 (2014).

[12] Q. Liu, X. Zhang, L. B. Abdalla, A. Fazzio, and A. Zunger, Switching a normal insulator into a topological insulator via electric field with application to phosphorene, Nano Lett. **15**, 1222 (2015).

[13] X. Peng, Q. Wei, and A. Copple, Strain-engineered direct-indirect band gap transition and its mechanism in two-dimensional phosphorene, Phys. Rev. B **90**, 085402 (2014).

[14] A. Ziletti, A. Carvalho, P. E. Trevisanutto, D. K. Campbell, D. F. Coker, and A. H. Castro Neto, Phosphorene oxides: Bandgap engineering of phosphorene by oxidation, Phys. Rev. B **91**, 085407 (2015).

[15] Z. Y. Ong, Y. Cai, G. Zhang, and Y. W. Zhang, Strong thermal transport anisotropy and strain modulation in single-layer phosphorene, J. Phys. Chem. C **118**, 25272 (2014).

[16] L. Zhu, G. Zhang, and B. Li, Coexistence of size-dependent and size-independent thermal conductivities in phosphorene, Phys. Rev. B **90**, 214302 (2014).

[17] Y. Hong, J. Zhang, X. Huang, and X. C. Zeng, Thermal conductivity of a two-dimensional phosphorene sheet: A comparative study with graphene, Nanoscale **7**, 18716 (2015).

[18] G. Qin, Q. B. Yan, Z. Qin, S. Y. Yue, M. Hu, and G. Su, Anisotropic intrinsic lattice thermal conductivity of phosphorene from first principles, Phys. Chem. Chem. Phys. **17**, 4854 (2015).

[19] A. Jain and A. J. H. McGaughey, Strongly anisotropic in-plane thermal transport in single-layer black phosphorene, Sci. Rep. **5**, 8501 (2015).

[20] G. Zhang, and Y.-W. Zhang, Thermal properties of two-dimensional materials, Chin. Phys. B **26**, 034401 (2017).

[21] Y. Hong, J. Zhang, and X. C. Zeng, Thermal transport in phosphorene and phosphorene-based materials: A review on numerical studies, Chin. Phys. B **27**, 036501 (2018).

[22] B. Smith, B. Vermeersch, J. Carrete, E. Ou, J. Kim, N. Mingo, D. Akinwande and L. Shi, Temperature and thickness dependences of the anisotropic in-plane thermal conductivity of black phosphorus, Adv. Mater. **29**, 1603756 (2017).

[23] J. Chen, J. He, D. Pan, X. Wang, N. Yang, J. Zhu, S. A. Yang, and G. Zhang, Emerging theory and phenomena in thermal conduction: A selective review, Sci. China Phys. Mech. Astron. **65**, 117002 (2022).

[24] Y. Cheng, X. Wu, Z. Zhang, Y. Sun, Y. Zhao, Y. Zhang, and G. Zhang, Thermo-mechanical correlation in two-dimensional materials, Nanoscale **13**, 1425 (2021).

[25] J. Wu, Y. Chen, J. Wu, and K. Hippalgaonkar, Perspectives on thermoelectricity in layered and 2D materials, Adv. Electron. Mater. **4**, 1800248 (2018).

[26] C. Sevik and H. Sevinçli, Promising thermoelectric properties of phosphorenes, Nanotechnology **27**, 355705 (2016).

[27] B. Zhu, Q. Chen, S. Jiang, M. Holt, W. Zhu, D. Akinwande, and L. Tao, Thermoelectric effect and devices on IVA and VA Xenes, InfoMat **3**, 271 (2021).

[28] S. Lee, F. Yang, J. Suh, S. Yang, Y. Lee, G. Li, H. S. Choe, A. Suslu, Y. Chen, C. Ko, J. Park, K. Liu, J. Li, K. Hippalgaonkar, J. J. Urban, S. Tongay, J. Wu, Anisotropic in-plane thermal conductivity of black phosphorus nanoribbons at temperatures higher than 100 K, Nat. Commun. **6**, 8573 (2015).

[29] H. Liu, H. Sung Choe, Y. Chen, J. Suh, C. Ko, S. Tongay, J. Wu, Variable range hopping electric and thermoelectric transport in anisotropic black phosphorus, Appl. Phys. Lett. **111**, 102101 (2017).

[30] Y. Saito, T. Iizuka, T. Koretsune, R. Arita, S. Shimizu, Y. Iwasa, Gate-tuned thermoelectric power in black phosphorus, Nano Lett. **16**, 4819 (2016).

[31] R. Fei, A. Faghaninia, R. Soklaski, J. A. Yan, C. Lo, L. Yang, Enhanced thermoelectric efficiency via orthogonal electrical and thermal conductances in phosphorene, Nano Lett. **14**, 6393 (2014).

[32] H. Y. Lv, W. J. Lu, D. F. Shao, Y. P. Sun, Large thermoelectric power factors in black phosphorus and phosphorene, arXiv:1404.5171.

[33] M. Zare, B. Z. Rameshti, F. G. Ghamsari, and R. Asgari, Thermoelectric transport in monolayer phosphorene, Phys. Rev. B **95**, 045422 (2017).

[34] H. D. Bui and M. Yarmohammadi, Direction-dependent electronic thermal conductivity and thermopower of single-layer black phosphorus in the presence of bias voltage and dilute charged impurity, Phys. E **103**, 76 (2018).

[35] H. Y. Lv, W. J. Lu, D. F. Shao and Y. P. Sun, Enhanced thermoelectric performance of phosphorene by strain-induced band convergence, Phys. Rev. B **90**, 085433 (2014).

[36] S. Konabe, and T. Yamamoto, Significant enhancement of the thermoelectric performance of phosphorene through the application of tensile strain, Appl. Phys. Express **8**, 015202 (2015).

[37] J. Zhang, H. J. Liu, L. Cheng, J. Wei, J. H. Liang, D. D. Fan, J. Shi, X. F. Tang, and Q. J. Zhang, Phosphorene nanoribbon as a promising candidate for thermoelectric applications, Sci. Rep. **4**, 6452 (2014).

[38] R. Ma, H. Geng, W. Y. Deng, M. N. Chen, L. Sheng, and D. Y. Xing, Effect of the edge states on the conductance and thermopower in zigzag phosphorene nanoribbons, Phys. Rev. B **94**, 125410 (2016).

[39] H. Zhu, Even–odd effect of the thermoelectric information for zigzag phosphorene nanoribbons under an electric field, Physica B **605**, 412774 (2021).

[40] B. Zhou, J. Yuan, X. Zhou and B. Zhou, Even–odd effect of spin-dependent transport and thermoelectric properties for ferromagnetic zigzag phosphorene nanoribbons under an electric field, J. Phys.: Condens. Matter **32**, 435502 (2020).

[41] H. Zhou, Y. Cai, G. Zhang, and Y. W. Zhang, Thermoelectric properties of phosphorene at the nanoscale, J. Mater. Res. **31**, 3179 (2016).

[42] L. Medrano-Sandonas, D. Teich, R. Gutierrez, T. Lorenz, A. Pecchia, G. Seifert, and G. Cuniberti, Anisotropic Thermoelectric Response in Two-Dimensional Puckered Structures, J. Phys. Chem. C **120**, 18841 (2016).

[43] Y. Tanaka, M. Saito and F. Ishii, Anisotropic thermoelectric effect on phosphorene and bismuthene: First-principles calculations based on nonequilibrium Green's function theory, Jpn. J. Appl. Phys., Part 1 **57**, 125201 (2018).

[44] J. E. Padilha, A. Fazzio, and A. J. R. da Silva, Van der Waals Heterostructure of Phosphorene and Graphene: Tuning the Schottky Barrier and Doping by Electrostatic Gating, Phys. Rev. Lett. **114**, 066803 (2015).

[45] A. Avsar, I. J. Vera-Marun, J. Y. Tan, K. Watanabe, T. Taniguchi, A. H. Castro Neto, and B. Özyilmaz, Air-stable transport in graphene-contacted, fully encapsulated ultrathin black phosphorus-based field-effect transistors, ACS Nano **9**, 4138 (2015).

[46] S. Molina-Valdovinos, K. J. Lamas-Martínez, J. A. Briones-Torres and I. Rodríguez-Vargas, Electronic cloaking of confined

states in phosphorene junctions, J. Phys.: Condens. Matter **34**, 195301 (2022).

[47] Y. Betancur-Ocampo, F. Leyvraz, and T. Stegmann, Electron optics in phosphorene pn junctions: Negative reflection and anti-super-klein tunneling, Nano Lett. **19**, 7760 (2019).

[48] H. Hedayati Kh, and E. Faizabadi, Dwell time, Hartman effect and transport properties in a ferromagnetic phosphorene monolayer, J. Phys.: Condens. Matter **30**, 085303 (2018).

[49] R. Biswas, and C. Sinha, Quenching effect of oscillating potential on anisotropic resonant transmission through a phosphorene electrostatic barrier, Sci. Rep. **11**, 2881 (2021).

[50] S. Dana, M. Zare, and P. Zamani, Charge transport in nnn and npn phosphorene junctions: The use of phosphorene pn junctions as rectifiers, Physica E **124**, 114239 (2020).

[51] J. Jia, S. Jeon, J. Jeon, J.-H. Park, and S. Lee, Versatile doping control of black phosphorus and functional junction structures, J. Phys. Chem. C **123**, 10682 (2019).

[52] D.-K. Kim, S.-B. Hong, K. Jeong, C. Lee, H. Kim, and M.-H. Cho, P-N junction diode using plasma boron-doped black phosphorus for high-performance photovoltaic devices, ACS Nano **13**, 1683 (2019).

[53] T. Vincent, J. Liang, S. Singh, E. G. Castanon, X. Zhang, A. McCreary, D. Jariwala, O. Kazakova, and Z. Y. Al Balushi, Opportunities in electrically tunable 2D materials beyond graphene: Recent progress and future outlook, Appl. Phys. Rev. **8**, 041320 (2021).

[54] Y. Betancur-Ocampo, E. Paredes-Rocha, and T. Stegmann, Phosphorene pnp junctions as perfect electron waveguides, J. Appl. Phys. **128**, 114303 (2020).

[55] M. Ezawa, Topological origin of quasi-flat edge band in phosphorene, New J. Phys. **16**, 115004 (2014).

[56] V. L. A. Margulis, E. E. Muryumin, and E. A. Gaiduk, Optical reflection, transmission and absorption properties of single-layer black phosphorus from a model calculation, J. Opt. **18**, 055102 (2016).

[57] J. A. Briones-Torres, R. Pernas-Salomón, R. Pérez-Álvarez, and I. Rodríguez-Vargas, Hybrid matrix method for stable numerical analysis of the propagation of Dirac electrons in gapless bilayer graphene superlattices, Superlattices Microstruct. **93**, 186-201 (2016).

[58] R. Pérez-Álvarez and F. García-Moliner, *Transfer Matrix, Green Function and Related Techniques: Tools for Study of Multilayer Heterostructures* (Universitat Jaume I, Castellon de la Plana Spain, 2004).

[59] R. Pernas-Salomón and R. Pérez-Alvarez, Sturm-liouville matrix equation for the study of electromagnetic-waves propagation in layered anisotropic media, Prog. Electromagn. Res. M **40**, 79 (2014).

[60] S. Datta, *Electronic Transport in Mesoscopic Systems* (Cambridge University Press, 1997).

[61] See Supplemental Material at http://link.aps.org/supplemental/ 10.1103/PhysRevB.107.245427 for the thermoelectric properties of GPJs: Mediated exclusively by electrons or $n-n-n$

transport, in the region of hole states inside the barrier for $n-p-n$ transport, for realistic parameters in the case of $n-p-n$ transport, and including the phononic contribution.

[62] N. Stojanovic, D. H. S. Maithripala, J. M. Berg, and M. Holtz, Thermal conductivity in metallic nanostructures at high temperature: Electrons, phonons, and the Wiedemann-Franz law, Phys. Rev. B **82**, 075418 (2010).

[63] J. Kim, S. S. Baik, S. H. Ryu, Y. Sohn, S. Park, B.-G. Park, J. Delinger, Y. Yi, H. J. Choi, and S. Kim, Observation of tunable band gap and anisotropic Dirac semimetal state in black phosphorus, Science **349**, 723 (2015).

[64] B. Deng, V. Tran, Y. Xie, H. Jiang, C. Li, Q. Guo, X. Wang, H. Tian, S. J. Koester, H. Wang, J. J. Cha, Q. Xia, L. Yang, and F. Xia, Efficient electrical control of thin-film black phosphorus bandgap, Nat. Commun. **8**, 14474 (2017).

[65] S. W. Jung, S. H. Ryu, W. J. Shin, Y. Sohn, M. Huh, R. J. Koch, C. Jozwiak, E. Rotenberg, A. Bostwick, and K. S. Kim, Black phosphorus as a bipolar pseudospin semiconductor, Nature Mater. **19**, 277 (2020).

[66] J. H. Seol, I. Jo, A. L. Moore, L. Lindsay, Z. H. Aitken, M. T. Pettes, X. Li, Z. Yao, R. Huang, D. Broido, N. Mingo, R. S. Ruoff, and L. Shi, Two-dimensional phonon transport in supported graphene, Science **328**, 213 (2010).

[67] Y. Ni, Y. Chalopin, and S. Volz, Few layer graphene based superlattices as efficient thermal insulators, Appl. Phys. Lett. **103**, 141905 (2013).

[68] H. G. Kim, K. D. Kihm, W. Lee, G. Lim, S. Cheon, W. Lee, K. R. Pyun, S. H. Ko, and S. Shin, Effect of graphene-substrate conformity on the in-plane thermal conductivity of supported graphene, Carbon **125**, 39 (2017).

[69] Z. Wang, T. Feng, and X. Ruan, Thermal conductivity and spectral phonon properties of freestanding and supported silicene, J. Appl. Phys. **117**, 084317 (2015).

[70] A. J. Gabourie, S. V. Suryavanshi, A. B. Farimani, and E. Pop, Reduced thermal conductivity of supported and encased monolayer and bilayer MoS_2, 2D Mater. **8**, 011001 (2021).

[71] G. Qin, Z. Qin, S.-Y. Yue, Q.-B. Yan, and M. Hu, External electric field driving the ultra-low thermal conductivity of silicene, Nanoscale **9**, 7227 (2017).

[72] S.-Y. Yue, R. Yang, and B. Liao, Controlling thermal conductivity of two-dimensional materials via externally induced phonon-electron interaction, Phys. Rev. B **100**, 115408 (2019).

[73] Z. Chang, K. Yuan, Z. Sun, X. Zhang, Y. Gao, G. Qin, and D. Tang, Ultralow lattice thermal conductivity and dramatically enhanced thermoelectric properties of monolayer InSe induced by an external electric field, Phys. Chem. Chem. Phys. **23**, 13633 (2021).

[74] D. Wei, E. Zhou, X. Zheng, H. Wang, C. Shen, H. Zhang, Z. Qin, and G. Qin, Electric-controlled tunable thermal switch based on Janus monolayer MoSSe, npj Comput. Mater. **8**, 260 (2022).

[75] E. Zhou, D. Wei, J. Wu, G. Qin, and M. Hu, Electrically driven robust tuning of lattice thermal conductivity, Phys. Chem. Chem. Phys. **24**, 17479 (2022).